Misoprostol Treatment Prevents Hypoxia-Induced Cardiac Dysfunction, Aberrant Cardiomyocyte Mitochondrial Dynamics and Permeability Transition Through Bnip3 Phosphorylation

Matthew D. Martens[1,7], Nivedita Seshadri[2,7], Lucas Nguyen[7], Donald Chapman[7], Elizabeth S. Henson[2,9], Bo Xiang[3,7], Arielys Mendoza[11], Sunil Rattan[4,10], Spencer B. Gibson[2,9], Ayesha Saleem[6,7], Grant M. Hatch[4,7], Christine A. Doucette[2,7], Jason M. Karch[11], Vernon W. Dolinsky[3,7], Ian M. Dixon[4,10], Adrian R. West[2,8], Christof Rampitsch[12], and Joseph W. Gordon[1,5,7,*]

Departments of Human Anatomy and Cell Science[1], Physiology and Pathophysiology[2], Biochemistry and Medical Genetics[3], Pharmacology and Therapeutics[4] and the College Nursing[5] in the Rady Faculty of Health Science, The Faculty of Kinesiology and Recreation Management[6]. The Diabetes Research Envisioned and Accomplished in Manitoba (DREAM) Theme[7] and the Biology of Breathing (BoB) Theme[8] of the Children's Hospital Research Institute of Manitoba, the Research Institute in Oncology and Hematology[9], and the Institute for Cardiovascular Sciences[10], at the University of Manitoba, Winnipeg, Canada. The Department of Molecular Physiology and Biophysics, Cardiovascular Research Institute, Baylor College of Medicine, Houston TX, USA[11]. Morden Research & Development Centre, Agriculture and Agri-Food Canada, Morden, MB, Canada[12].

Running title: Misoprostol Inhibits Cardiomyocyte Bnip3 Activity

Key words: Hypoxia, Bnip3, Calcium Signaling, Necrosis, Permeability Transition, Cardiomyocyte

*Corresponding Author:

Children's Hospital Research Institute of Manitoba,

Department of Human Anatomy and Cell Science

College of Nursing, Rady Faculty of Health Sciences,

University of Manitoba.

715 McDermot Avenue, Winnipeg

Phone: 204-474-1325; Fax: 204-474-7682

joseph.gordon@umanitoba.ca

Graphical Abstract:

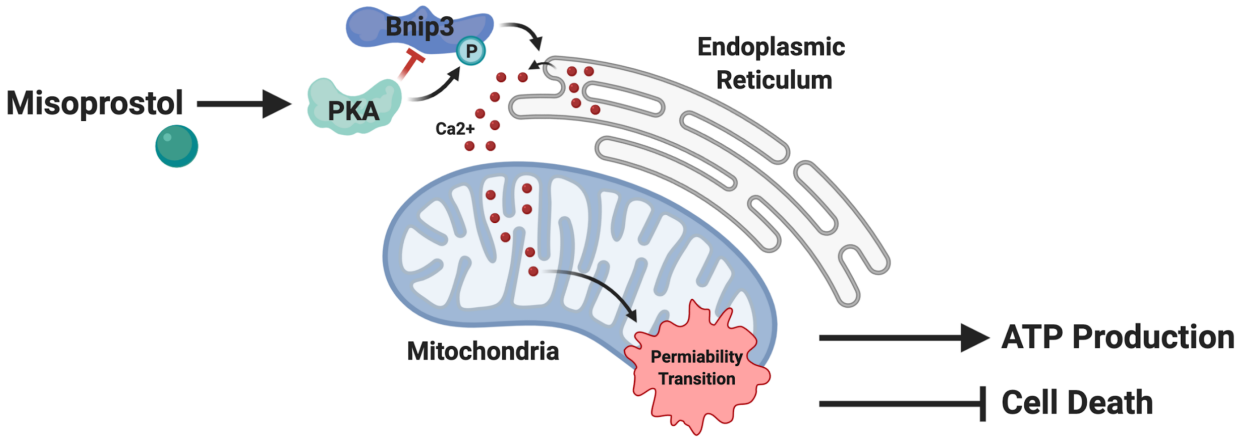

Abstract:

Systemic hypoxia, a major complication associated with reduced gestational time, affects more 60% of preterm infants and is a known driver of hypoxia-induced Bcl-2-like 19kDa-interacting protein 3 (Bnip3) expression in the neonatal heart. At the level of the cardiomyocyte, Bnip3 activity plays a prominent role in the evolution of necrotic cell death, disrupting subcellular calcium homeostasis and initiating mitochondrial permeability transition (MPT). Emerging evidence suggests both a cardioprotective role for protein kinase A (PKA) through stimulatory prostaglandin (PG) E1 signalling during prolonged periods of hypoxia, and a cytoprotective role for Bnip3 phosphorylation, indicating that post-translational modifications of Bnip3 may be a point of convergence for these two protective pathways. Using a combination of in vivo and multiple cell models, including human iPSC-derived cardiomyocytes, we tested if the PGE1 analogue misoprostol is cardioprotective during neonatal hypoxic injury by altering the phosphorylation status of Bnip3. Here we report that hypoxia exposure significantly increases Bnip3 expression, mitochondrial-fragmentation, -ROS, -calcium accumulation and -permeability transition, while reducing mitochondrial membrane potential, all of which were restored to control levels with the addition of misoprostol, despite elevated Bnip3 protein expression. Through both gain- and loss-of-function genetic studies we further show that misoprostol-induced protection directly affects Bnip3, preventing mitochondrial perturbations. We demonstrate that this is a result of PG EP4 receptor

signalling, PKA activation, and direct Bnip3 phosphorylation at threonine-181. Furthermore, when this PKA phosphorylation site within Bnip3 is neutralized, the protective misoprostol effect is lost. We also provide evidence that misoprostol traffics Bnip3 away from the ER through a physical interaction with 14-3-3β, thereby preventing aberrant ER calcium release and MPT. *In vivo* studies further demonstrate that misoprostol treatment increases Bnip3 phosphorylation at threonine-181 in the mouse heart, while both misoprostol treatment and genetic ablation of Bnip3 prevented hypoxia-induced reductions in contractile function. Taken together, our results demonstrate a foundational role for Bnip3 phosphorylation in the molecular regulation of cardiomyocyte contractile and metabolic dysfunction and identifies EP4 signaling as a potential pharmacological mechanism to prevent hypoxia-induced neonatal cardiac injury.

1. Introduction:

Globally, the preterm birth rate is 11.1%, meaning more than 15 million infants are born before 37 weeks of gestation each year, at the same time complications associated with preterm birth are recognized as the leading cause of death among children under age 5 (Blencowe *et al*, 2012; Liu *et al*, 2016). Systemic hypoxia, a major complication associated with reduced gestational time, affects more than 60% of preterm infants and is known to activate pathological hypoxia signalling across most neonatal tissues (Luu *et al*, 2015; Vannucci, 2004; Shastri *et al*, 2012). Moreover, stressors linked to hypoxic injury have been shown to alter neonatal cardiac metabolism, resulting in diminished contractile performance and compromised tissue perfusion, further compounding neuro-cognitive and end-organ complications (Armstrong *et al*, 2012). A lack of oxygen at the level of the cardiomyocyte results in the accumulation and activation of transcription factors belonging to the hypoxia-inducible factor-alpha (HIFα) family (Greer *et al*, 2012; Chaudhuri *et al*, 2020). This inducible pathway is conserved throughout life, functioning to drive the expression of a number of genes, and promoting cardiomyocyte glycolysis and diminishing mitochondrial respiration when oxygen tension is low (Greer *et al*, 2012; Chaudhuri *et al*, 2020; Carmeliet *et al*, 1998).

Bcl-2-like 19 kDa-interacting protein 3 (Bnip3) is one such hypoxia-inducible gene and is also a member of the pro-apoptotic BH3-only subfamily of the Bcl-2 family of proteins (Gustafsson, 2011; Field *et al*, 2018; Kubli *et al*, 2007; Azad *et al*, 2008; Gordon *et al*, 2011). Bnip3 is an atypical member of this subfamily, which classically use their BH3 domains to drive cell death, however Bnip3's pro-apoptotic functions are controlled through its C-terminal transmembrane (TM) domain (Ray *et al*, 2000). Previous studies indicate that through this functionally important domain, Bnip3 inserts through the outer mitochondrial membrane, interacting with optic atrophy-1 (OPA-1), driving mitochondrial bioenergetic collapse, fission, cytochrome c release and apoptosis (Ray *et al*, 2000; Liu & Frazier, 2015; Landes *et al*, 2010). Alternatively, Bnip3 can also localize to the endoplasmic reticulum (ER), interrupting Bcl-2-induced inhibition of inositol trisphosphate receptor (IP_3R) calcium leak, resulting in ER calcium depletion and mitochondrial matrix calcium accumulation, mediated though voltage-dependent anion channel (VDAC) and the mitochondrial calcium uniporter (MCU) (Ray *et al*, 2000; Zhang *et al*, 2009; Rapizzi *et al*, 2002; Baughman *et al*, 2011; Chaudhuri *et al*, 2013). Accumulating evidence suggests that elevated matrix calcium is an important trigger for mitochondrial permeability transition (MPT), a phenomena that is required for the induction of necrotic cell death and evolution of ischemic injury (Karch *et al*, 2013; Giorgio *et al*, 2013; Izzo *et al*, 2016; Mughal *et al*, 2018; Whelan *et al*, 2010; Baines *et al*, 2005; Nakagawa *et al*, 2005; Kwong *et al*, 2014). Key to both of these processes is Bnip3's ability to drive mitochondrial bioenergetic collapse by affecting complexes of the inner mitochondrial membrane's electron transport chain, and ultimately ATP production (Rikka *et al*, 2011). Taken together, these observations have long made Bnip3 an attractive therapeutic target in the heart, with limited success.

Interestingly, previous work has demonstrated that prostaglandin (PG) signalling through the PG EP4 receptor, a G-protein coupled receptor classically associated with enhanced protein kinase A (PKA) activity, improves cardiac function in mice following MI (Bryson *et al*, 2018). Furthermore, overexpression of the EP3 receptor, known to reduce PKA activity, is deleterious in the murine heart (Bryson *et al*, 2020). Recent work from our group built on this, demonstrating that misoprostol, a PGE1

analogue that is capable of binding to both EP3 and EP4 receptors, activated PKA signaling and was cytoprotective in an *in vitro* model of chronic hypoxia (Field *et al*, 2018). Moreover, loss of Bnip3 activity through ablation or overexpression of the dominant negative form of Bnip3 (Bnip3ΔTM) is protective in the heart or cultured myocytes, respectively following prolonged ischemic episodes (Regula *et al*, 2002; Hamacher-Brady *et al*, 2007; Kubasiak *et al*, 2002). Work in cell culture models has further concluded that Bnip3 TM-domain phosphorylation is cytoprotective by limiting Bnip3's activity at the mitochondria and inhibiting apoptosis (Liu & Frazier, 2015). However, it is not currently known if Bnip3 phosphorylation can be pharmacologically modulated to impact cardiomyocyte permeability transition and *in vivo* heart function during a hypoxic episode (Liu & Frazier, 2015). Based on these previous studies, we examined if prostaglandin signalling though misoprostol is sufficient to alter Bnip3 phosphorylation status in order to prevent mitochondrial calcium accumulation, and permeability transition in the neonatal heart.

In this report we provide novel evidence that through EP4 receptor signalling, misoprostol inhibits hypoxia-induced neonatal contractile dysfunction resultant from cardiomyocyte respiratory collapse. We further show that this is a result of inhibiting Bnip3-induced transfer of calcium from the ER to the mitochondria, which prevents mitochondrial dysfunction, ATP depletion, MPT and necrotic cell death. Mechanistically, we provide evidence that this process is regulated through PKA, by elucidating a PKA phosphorylation site on mouse Bnip3 at threonine-181, which we show is essential for the inhibition of Bnip3 protein activity. We further delineate a role for the 14-3-3 family of molecular chaperones in this novel pharmacological pathway, demonstrating that 14-3-3β interacts with Bnip3, facilitating misoprostol-induced Bnip3 trafficking from the ER and mitochondria, thereby preventing hypoxia- and Bnip3-induced changes in subcellular calcium localization and MPT.

2. Materials and Methods:

2.1. In Vivo Neonatal Hypoxia Model and Adult Coronary Ligation Model:

All procedures in this study were approved by the Animal Care Committee of the University of Manitoba, which adheres to the principles for biomedical research involving animals developed by the

Canadian Council on Animal Care (CCAC). Litters of wild-type and/or Bnip3-null (embryonic deletion described previously (Diwan *et al*, 2007)) C57BL/6 mouse pups and their dams were placed in a hypoxia chamber with 10% O_2 (±1%) from postnatal day (PND) 3-10. Control litters were left in normoxic conditions at 21% O_2. Animals received 10 µg/kg misoprostol or saline control, administered through subcutaneous injection daily from PND3-10. At PND10 animals were euthanized and perfused with saline for tissue collection. In the *in vivo* rodent model of myocardial infarction, the left coronary artery of Sprague Dawley rats was ligated approximately 2 mm from its origin, while sham operated rats serve as control (Dixon *et al*, 1990; Ghavami *et al*, 2015). Following recovery for 4 or 8 weeks, animals are anesthetized, the heart excised, and the left anterior descending territory dissected for scar tissue and viable border-zone myocardium.

2.2. In Vivo Assessment of Cardiac Function:

Transthoracic echocardiography was performed on mildly anesthetized rats (sedated with 3% isofluorane & 1.0 L/min oxygen and maintained at 1-1.5% isofluorane &1L/min oxygen) at 10 days of age using a Vevo 2100 High-Resolution Imaging System equipped with a 30-MHz transducer (RMV-716; VisualSonics, Toronto) as described previously (Dolinsky *et al*, 2010).

2.3 Cell Culture and Transfections:

Rat primary ventricular neonatal cardiomyocytes (PVNC) were isolated from 1-2-day old pups using the Pierce Primary Cardiomyocyte Isolation Kit (#88281), which includes a Cardiomyocyte Growth Supplement to reduce fibroblast contamination. H9c2 cells were maintained in Dulbecco's modified Eagle's medium (DMEM; Hyclone), containing penicillin, streptomycin, and 10% fetal bovine serum (Hyclone), media was supplemented with MEM Non-Essential Amino Acids Solution (Gibco) for MEFs, cells were incubated at 37 °C and 5% CO2. Human induced pluripotent stem cell derived cardiomyocytes (H-iPSC-CMs) were obtained from Cellular Dynamics (iCell Cardiomyocytes #01434). iCell Cardiomyocytes were cultured in maintenance medium as per manufacturer's protocol and differentiated for 72 hours. Cell lines were transfected using JetPrime Polyplus reagent, as per the manufacturer's protocol. For misoprostol treatments, 10 mM misoprostol (Sigma) in phosphate buffered saline (PBS;

Hyclone) was diluted to 10 μM directly in the media and applied to cells for 24 hours. For hypoxia treatments, cells were held in a Biospherix incubator sub-chamber with 1% O_2 (±1%), 5% CO_2, balanced with pure N_2 (regulated by a Biospherix ProOx C21 sub-chamber controller) at 37 °C for 24 hours. BvO2, L161-982, L798-106, and H89 dihydrochloride (H89) were purchased from Sigma. RNAi experiments targeting Bnip3, including the generation of si-Bnip3 were described previously (Field *et al*, 2018).

2.4 Plasmids:

Mito-Emerald (mEmerald-Mito-7) was a gift from Michael Davidson (Addgene #54160) (Planchon *et al*, 2011). The endoplasmic reticulum (CMV-ER-LAR-GECO1), and mitochondrial (CMV-mito-CAR-GECO1) targeted calcium biosensors were gifts from Robert Campbell (Addgene #61244, and #46022) (Wu *et al*, 2013). CMV-dsRed was a gift from John C. McDermott. The FRET-based ATP biosensor (ATeam1.03-nD/nA/pcDNA3) was a gift from Takeharu Nagai (Addgene plasmid #51958) (Kotera *et al*, 2010). The dimerization-dependent PKA biosensor (pPHT-PKA) was a gift from Anne Marie Quinn (Addgene #60936) (Ding *et al*, 2015). pcDNA3-HA-14-3-3 beta (14-3-3β) was a gift from Michael Yaffe (Addgene #13270). The generation of mouse myc-Bnip3 (Addgene #100796) was described previously (Diehl-Jones *et al*, 2015). The phospho-neutral mouse myc-Bnip3-T181A was generated by PCR using the New England Biolabs Q5 Site-Directed Mutagenesis Kit and primers Forward: 5'-CTAGTCTAGA ATGTCGCAGAGCGGGGAGGAGAAC-3'and Reverse: 5'-GATCGGATCCTCAGAAGGTGCTAGTGGAAGTtgcCAG-3'.

2.5 Fluorescent Staining, Live Cell Imaging and Immunofluorescence:

MitoView Green, TMRM, Calcein-AM, ethidium homodimer-1, and Hoechst 33342 were purchased from Biotium. MitoSox was purchased from Life Technologies. MPTP imaging was described previously (Mughal *et al*, 2018). Dye based calcium imaging was done with Rhod-2AM (Invitrogen, R1245MP) as per manufacturer's protocol (including the production of dihyrdorhod-2 AM). Immunofluorescence with HMBG1 (CST # 3935), rodent specific Bnip3 (CST # 3769), TOM-20 (CST # 42406), and SERCA (Sigma MA3-919) antibodies were performed in conjunction with fluorescent secondary antibodies conjugated to Alexa Fluor 466 or 647 (Jackson). All epifluorescent imaging

experiments were done on a Zeiss Axiovert 200 inverted microscope fitted with a Calibri 7 LED Light Source (Zeiss) and Axiocam 702 mono camera (Zeiss) in combination with Zen 2.3 Pro imaging software. Confocal imaging was done on a Zeiss LSM700 Spectral Confocal Microscope in combination with Zen Black, which was also used for colocalization analysis, while FRET imaging was done using a Cytation 5 Cell Imaging Multi-Mode Reader. Quantification, scale bars, and processing including background subtraction, was done on Fiji (ImageJ) software.

2.6. Transmission Electron Microscopy (TEM):

TEM imaging was performed according to a protocol described previously (Moghadam *et al*, 2018). Briefly, PND10 hearts were fixed (3% glutaraldehyde in PBS, pH 7.4) for 3 hours at room temperature. Hearts were treated with a post-fixation step using 1% osmium tetroxide in phosphate buffer for 2 hours at room temperature, followed by an alcohol dehydration series before embedding in Epon. TEM was performed with a Philips CM10, at 80 kV, on ultra-thin sections (100 nm on 200 mesh grids). Hearts were stained with uranyl acetate and counterstained with lead citrate.

2.7. Immunoblotting:

Protein isolation and quantification was performed as described previously (Field *et al*, 2018). Extracts were resolved via SDS-PAGE and later transferred to a PVDF membrane using an overnight transfer system. Immunoblotting was carried out using primary antibodies in 5% powdered milk or BSA (as per manufacturer's instructions) dissolved in TBST. Horseradish peroxidase-conjugated secondary antibodies (Jackson ImmunoResearch Laboratories; 1:5000) were used in combination with enhanced chemiluminescence (ECL) to visualize bands. The following antibodies were used: HMGB1 (CST # 3935), Rodent-specific Bnip3 (CST # 3769), Myc-Tag (CST # 2272), HA-Tag (CST # 3724), Actin (sc-1616), and Tubulin (CST #86298). For detection of phosphorylation of Bnip3 at threonine-181, a custom rabbit polyclonal antibody was generated by Abgent using the following peptide sequence: AIGLGIYIGRRLp(T)TSTSTF.

2.6. Quantitative PCR:

Total RNA was extracted from pulverized frozen tissue or from cultured cells by TRIzol method. cDNA was generated using SuperScript IV VILO Master Mix with ezDNase (Thermo #11766050) and q-RT-PCR performed using TaqMan Fast Advanced master mix (Thermo #4444965) on a CFX384 Real-Time PCR Instrument. The primers used were provided through ThermoFisher custom plating arrays (see supplement 1 and 2 for assay list).

2.7. Cardiac and Cellular Lactate, ATP and Extracellular Acidification:

Cardiac lactate was quantified using the bioluminescent Lactate-Glo™ Assay (Promega #J5021) in deproteinized PND10 heart samples, as per the manufacturer's protocol. Luminescence was detected and quantified using a Fluostar Optima microplate reader (BMG Labtech, Ortenberg, Germany). Cardiac and H9c2 ATP content was determined using a the Adenosine 5′-triphosphate (ATP) Bioluminescent Assay Kit (Sigma #FLAA-1KT), and normalized to DNA content as described previously (Seshadri *et al*, 2017). Extracellular acidification and oxygen consumption was determined on a Seahorse XF-24 Extracellular Flux Analyzer in combination with Seahorse Mitochondrial Stress Test with drug concentrations as follows: 1 uM Oligomycin, 2 uM FCCP and 1uM Rotanone/Antimycin A (Agilent Seahorse #103015-100). Calculated oxygen consumption rates were determined as per manufacturer's instructions (Mitochondrial Stress Test; Seahorse).

2.8. Mitochondrial Swelling and CRC Assays:

Heart mitochondria were isolated by homogenization followed by differential centrifugation. Hearts were prepared with a Teflon homogenizer, while cells were disrupted with a glass homogenizer. The isolation buffer consisted of 250 mM sucrose and 10 mM Tris pH 7.4. Mitoplasts were isolated by incubating the isolated mitochondria in a hypotonic buffer, which consisted of 10 mM KCl, 10 mM Tris pH 7.4 for 20 min followed by gentle agitation with a pipette, and a low-speed centrifugation. Mitochondrial swelling and calcium retention capacity experiments were performed simultaneously using a dual-detector (one to measure fluorescence and the other to measure absorbance), single-cuvette–based fluori- metric system (Horiba Scientific) as described previously (Karch *et al*, 2019).

2.9. Phospho Peptide Mapping:

Synthetic peptides (GeneScript) were resuspended at a concentration of 1 mg/ml. These peptides were used as the substrate in a PKA kinase assay kit (New England Biolabs, #P6000S) according to the manufacturer's instructions, with the exception that [32P]-ATP was replaced with fresh molecular biology grade ATP. The Kemptide substrate (Enzo Life Sciences; #P-107; LRRASLG) was used as a positive control in each assay. Before mass spectrometry analysis, kinase assays were prepared using C18 ZipTips (EMD Millipore, Etobicoke, ON, Canada). Samples in 50% acetonitrile and 0.1% formic acid were introduced into a linear ion-trap mass spectrometer (LTQ XL: ThermoFisher, San Jose, CA, USA) via static nanoflow, using a glass capillary emitter (PicoTip: New Objective, Woburn, MA, USA), as described previously (Mughal *et al*, 2015).

2.10. Statistics:

Data are presented as mean ± standard error (S.E.M.) from 3 independent cell culture experiments. Differences between groups in imaging experiments with only 2 conditions were analyzed using an unpaired t-test, where (*) indicates $P<0.05$ compared with control. Experiments with 4 or more conditions were analyzed using a 1-way ANOVA, or 2-way ANOVA where appropriate, with subsequent Tukey test for multiple comparisons, where (*) indicates $P<0.05$ compared with control, and (**) indicates $P<0.05$ compared with treatment. All statistical analysis was done using GraphPad Prism software.

3. Results:

3.1. Misoprostol prevents hypoxia-induced contractile and mitochondrial dysfunction in vivo.

While clinical data suggests that preterm birth and neonatal hypoxia are major drivers of cardiac dysfunction, we were first interested in determining if we could replicate this using our previously described model of neonatal hypoxia, combined with daily misoprostol drug treatments from postnatal day (PND) 3-10 (Field *et al*, 2018; Martens *et al*, 2020). In our model, transthoracic echocardiography demonstrated signs of significant contractile dysfunction in hypoxia exposed PND10 animals, which included reductions in both fractional shortening (FS) and ejection fraction (EF), alongside considerable alterations in the ability for the left ventricle to fill properly in between beats (E'/A') (Fig. 1 A-C). We also observed that when

hypoxic animals were concurrently treated with misoprostol, contractility and filling of the heart returned to normoxic control levels (Fig. 1 A-C).

In an effort to understand the underlying mechanism of this dysfunction, we ran targeted PCR arrays to assess the expression of genes associated with mitochondrial energy metabolism and various cell death pathways (Fig. 1 D). Through this approach we found that there was dysregulation of genes associated with the mitochondrial electron transport chain (ETC), in particular there was a downregulation of genes associated with complex-1 (NADH ubiquinone oxidoreductase) (Fig.1 D), a phenomena which has previously been linked to mitochondrial dysfunction, fragmentation and bioenergetic collapse (Rikka *et al*, 2011). Additionally, we observed that genes associated with ATP synthase, the terminal step of electron transport and main beneficiary of a well developed proton motive force, were also down regulated in the PND10 hypoxic heart, relative to normoxic control animals (Fig. 1 D). When we examined cell death pathways, we found that a number of regulators of apoptosis and necrosis were down regulated, including: induced myeloid leukemia cell differentiation protein (Mcl-1), Ras-Related Protein Rab-25 (Rab25), CASP8 and FADD Like Apoptosis Regulator (Cflar), and cyclophilin D (Cyld) (Fig. 1D). At the same time hypoxia increased the expression of genes that drive extrinsic cell death and inflammation like, Tumor Necrosis Factor Receptor Superfamily Member 5 (CD40), Fas Cell Surface Death Receptor (Fas), TNF Receptor Associated Factor 2 (Traf2), DNA Fragmentation Factor Subunit Alpha (Dffa) and interleukins (IL) 17a and 12a (Fig. 1 D). Given the central role of Bnip3 in hypoxia-induced cell stress, and connections to mitochondrial energy metabolism and cell death, we also assessed its expression by Western blot analysis and observed that Bnip3 expression is significantly increased in the hypoxia-exposed PND10 heart (Fig. 1 E).

We were interested in determining if the PND10 heart was demonstrating signs of mitochondrial dysfunction. To do this, we assessed cardiac ATP content, and observed that after 7 days of 10% oxygen exposure there is a significant reduction in accumulated ATP in the neonatal heart (Fig. 1 F). Importantly, when we combined hypoxia and misoprostol drug treatments in these animals, ATP content was elevated significantly beyond normoxic control levels (Fig. 1 F). In keeping with a potential failure in oxidative

phosphorylation, we next assessed lactate content in the PND10 heart using a bioluminescent assay. In doing this, we found the opposite of what we observed with ATP in that there was a 33% increase in lactate concentration in hypoxia-exposed animals, when compared to control (Fig. 1G). Similarly though, daily misoprostol drug treatments during the hypoxia exposure was sufficient to significantly reduce lactate production in the PND10 mouse heart (Fig. 1 G). Next, we used transmission electron microscopy (TEM) to visualize mitochondrial morphology in the hypoxia-exposed neonatal mouse heart. This analysis revealed that hypoxia exposure results in both reduced mitochondrial size and altered structure when compared to the normoxic control, however this was absent with the addition of misoprostol treatment (Fig.1 H).

Together these results indicate that the hypoxia exposed PND10 heart may be undergoing bioenergetic collapse and early signs of cell death, resulting in significant alterations in contractile function concurrent with elevated Bnip3 expression.

3.2. Misoprostol prevents hypoxia-induced mitochondrial dysfunction in rodent and human cardiomyocytes.

In order to investigate if misoprostol can modulate hypoxia-induced mitochondrial dysfunction at the cellular level, we employed cultured primary ventricular neonatal cardiomyocytes (PVNCs), isolated from PND 1–2 rat pups. When exposed to hypoxia for 24-h we observed a significant increase in mitochondrial fragmentation when compared to normoxic control cells (Fig. 2 A, B), consistent with our TEM data, and commonly associated with mitochondrial dysfunction and complex-1 deficiency. However, when PVNCs were concurrently exposed to hypoxia and treated with misoprostol, fragmentation was absent and mitochondria returned to their normal branching and networked appearance (Fig. 2 A, B). Due to the previously reported association between fragmentation and mitochondrial dysfunction, we next performed a number of functional assays to assess PVNCs mitochondrial response to hypoxia. To do this we used TMRM, a cell-permeant red fluorescent dye to assess mitochondrial membrane potential ($\Delta\Psi m$). Through the application of this dye, we observed that hypoxia exposure significantly reduces $\Delta\Psi m$ when compared to normoxic controls, which was restored by misoprostol treatment (Fig. 2 C). We were further interested in determining if this observation translated to hypoxia-exposed human induced pluripotent stem

cell (IPSC)-derived cardiomyocytes (H-iPSC-CMs). Using this model, we observed that hypoxia exposure significantly reduces mitochondrial membrane potential in these human cells, and misoprostol is able to rescue this effect, consistent with the PVNC results (Fig. 2 D, E). We next moved to assess the production of mitochondrial derived superoxide, a common and potent cytotoxic free radical, using MitoSOX staining. We observed that hypoxia exposure markedly increases mitochondrial superoxide production well above that of control levels but is completely abrogated in the presence of misoprostol (Fig. 2 F, G).

Next, we investigated how hypoxia alters subcellular calcium dynamics and impacts mitochondrial permeability transition. To do this, we stained cardiomyocytes with a reduced form of Rhod-2AM (dihydrorhod2-AM), which provides specificity for mitochondrial calcium imaging. We observed that 24-h hypoxia exposure significantly increases mitochondrial calcium above that of normoxic control levels in both PVNCs and H-iPSC-CM's (Fig. 2 H-J). However, when hypoxic cardiomyocytes were co-treated with misoprostol, this hypoxia-induced mitochondrial calcium accumulation was prevented (Fig. 2 H-J). Given the previously published links between mitochondrial calcium accumulation and MPT, we assessed MPT in hypoxic cardiomyocytes using the calcein-$CoCl_2$ method [8,15,30]. Consistent with the calcium results, hypoxia exposure resulted in a loss of mitochondrial puncta, indicative of permeability transition, while cells that were concurrently treated with hypoxia and misoprostol maintained mitochondrial staining comparable to control levels (Fig. 2 K). Using extracellular flux analysis, we wanted to determine if this mitochondrial dysfunction had a physiological impact on oxidative-phosphorylation. As shown in Figure 2 L, myocyte hypoxia exposure significantly reduces basal, maximal and spare respiratory capacity, which further resulted in a significant reduction in mitochondrial ATP production. However, consistent with what was seen *in vivo*, the addition of misoprostol during hypoxia exposure abrogated this effect, preventing respiratory collapse in primary neonatal cardiomyocytes (Fig. 2 L).

While these results demonstrate that hypoxia exposure results in mitochondrial dysfunction, we also wanted to determine if the downstream result was ultimately cell death. In order to do this we performed live/dead assays using ethidium homodimer-1 to mark nuclei of cells that had lost their membrane integrity, a common characteristic of necrotic cell death (Galluzzi *et al*, 2018). With this

approach we observed that hypoxia exposure significantly increased the percentage of red staining nuclei by 173% when compared to normoxic control, however myocytes treated with misoprostol displayed levels of cell death similar to that of control cells (Fig. 2 M). To further understand the underlying mechanism of cell death in hypoxia-induced cardiomyocyte pathology we also assessed high mobility group box 1 (HMGB1) localization, a commonly used biomarker in the detection of necrosis. Using immunofluorescence, hypoxia exposed PVNCs demonstrated a significant decrease in HMGB1 nuclear localization, concurrent with an increase in secreted HMGB1 in the culture media (Fig. 2 N, O, P). Consistent with the live/dead results, the addition of misoprostol during hypoxia restored HMGB1 to the nucleus and further decreased its presence in the media, returning it back to control levels (Fig. 1 N, O, P). Taken together, these results indicate that misoprostol prevents hypoxia-induced mitochondrial dysfunction, and necrotic cell death of neonatal cardiomyocytes.

3.3. Misoprostol prevents Bnip3-induced mitochondrial dysfunction and cell death.

Given the central role that Bnip3 has previously been shown to play in the evolution of hypoxic injury in the heart, we also wanted to assess its expression in our model (Regula *et al*, 2002; Field *et al*, 2018). Using PVNCs we observed that hypoxia exposure was sufficient to drive the accumulation of Bnip3 (Fig. 3 A, B). Consistent with our previously published results, the addition of misoprostol in hypoxia-exposed PVNCs results in a reduction of Bnip3 protein expression, however it still remained elevated beyond the levels observed in the normoxic control cells (Fig. 3 A, B) (Field *et al*, 2018).

To determine if a direct link existed between hypoxia-induced alterations in mitochondrial function and Bnip3 protein expression, we used fibroblasts isolated from mouse embryos possessing a genetic deletion for Bnip3, described previously (Azad *et al*, 2008; Diwan *et al*, 2007). Using western blot analysis we observed that hypoxia exposure resulted in the induction of Bnip3 protein expression in the WT cells, but that this response was completely absent in the Bnip3-null MEFs (Fig. 3 C). TMRM analysis revealed that in WT MEFs hypoxia was sufficient to significantly reduce $\Delta\Psi m$ when compared to normoxic control cells, a phenomena that was absent in the $Bnip3^{-/-}$ MEFs (Fig. 3 D). Importantly, misoprostol treatment restored membrane potential in WT MEFs (Fig. 3 D). We next assessed

mitochondrial calcium accumulation using dihydrorhod2-AM, and observed that hypoxia increased mitochondrial calcium in the WT MEFs, but this response was absent in the Bnip3$^{-/-}$ MEFs. Consistent with our PVNC results, misoprostol provided protection against mitochondrial calcium accumulation in the WT cells (Fig. 3 E, F). In addition, Bnip3-null MEFs were less susceptible to hypoxia-induced MPT compared to WT MEFs, which demonstrated a significant reduction in mitochondrial puncta in response to hypoxia, which was restored by misoprostol treatment (Fig. 2 G).

Given that Bnip3 protein expression is elevated in our cellular model of hypoxia, we next wanted to determine if misoprostol had a direct effect on Bnip3. We used gain-of-function transfection studies in H9c2 cells and assessed markers of mitochondrial dysfunction. H9c2 cells were transfected with Bnip3, or empty vector control, along with mito-Emerald to visualize mitochondrial morphology. Shown in Figure 3 H and I, Bnip3 expression significantly alters mitochondrial morphology, resulting in a more fragmented appearance overall. Importantly when Bnip3-expressing cells were treated with misoprostol this effect was lost and mitochondria retained a branching and networked appearance (Fig. 3 H, I). Using TMRM we observed that Bnip3 expression induced mitochondrial depolarization, resulting in a 43% reduction in $\Delta\Psi m$ when compared to control (Fig. 3 J, K). However, when cells were treated with misoprostol, this effect was lost, returning $\Delta\Psi m$ to control (Fig. 3 J, K).

We next investigated the underlying mechanism of Bnip3-induced mitochondrial dysfunction, focusing on the role of subcellular calcium. To do this we employed organelle-targeted genetically-encoded calcium biosensors (GECOs) that fluoresce red in the presence of calcium. When we expressed the ER-targeted calcium biosensors (ER-LAR-GECO) in H9c2 cells we observed that Bnip3 expression significantly reduces ER calcium stores, when compared to control (Fig. 3 L, M). Concurrently, data generated using the mitochondrial targeted calcium indicator (Mito-CAR-GECO) demonstrated a Bnip3-dependent increase in mitochondrial calcium (Fig. 3 N, O). Together this data suggests that Bnip3-induced a shift of calcium from the ER to the mitochondria, consistent with previous observations in a neuronal cell line (Zhang *et al*, 2009). We further demonstrate that this shift in calcium is completely prevented in the presence of misoprostol, indicating a role for misoprostol in Bnip3 inhibition upstream of the ER (Fig. 3 L-

O). We also evaluated if Bnip3-induced mitochondrial calcium accumulation was impacting MPT. Using calcein staining with cobalt chloride, we observed that Bnip3 protein expression significantly reduces the number of cells with mitochondrial puncta by nearly 30%, indicating that MPT was actively occurring in these cells (Fig.3 P). In addition, we confirmed that misoprostol is capable of preventing Bnip3-induced MPT in H9c2 cells (Fig. 2 P).

Next, we determined if Bnip3-induced mitochondrial dysfunction led to a depletion of cellular ATP stores and bioenergetic collapse. Using the FRET-based ATeam biosensor to detect cytosolic ATP levels (Kotera *et al*, 2010), we observed that ATP content was significantly reduced in Bnip3-expressing H9c2 cells and that this effect was completely reversed in misoprostol treated cells (Fig. 3 Q). Complementary to what we observed with acute hypoxia exposure, Bnip3-induced mitochondrial dysfunction and bioenergetic collapse in H9c2 cells translated into a significant increase in the number dead cells per field, which was also prevented with misoprostol treatment (Fig. 3 R). Together this data indicates that misoprostol is capable of inhibiting Bnip3 protein activity and restoring mitochondrial calcium homeostasis.

3.4. Misoprostol modulates a novel PKA phosphorylation site on Bnip3 at Thr-181.

Next, we sought to determine if misoprostol was acting directly on the mitochondria or if a plasma membrane mediator was involved in this response. To do this we used isolated mitochondria from the whole rat heart, in combination with mitochondrial calcium retention capacity (CRC) and mitochondrial swelling assays that were treated directly with misoprostol or vehicle. Shown in Figure 4A and -B, misoprostol treatment had no effect on the calcium retention capacity or the optical absorbance of isolated mitochondria treated with exogenous calcium.

As misoprostol did not affect mitochondrial swelling or calcium accumulation directly, we investigated the role of prostaglandin cell surface receptors. We differentially inhibited the prostaglandin EP_3 and EP_4 receptors, which are both known to be enriched in the heart. Using TMRM to monitor $\Delta\Psi m$, we applied L161,982, a small molecule inhibitor of the EP_4 receptor, in combination with hypoxia and misoprostol treatments. Consistent with our observations in PVNCs, misoprostol treatment prevented hypoxia-induced mitochondrial depolarization, but importantly this rescue was completely lost when the

EP_4 receptor was inhibited (Fig. 4 C, D). Conversely, inhibition of the EP_3 receptor with L798106 had no effect on misoprostol's ability to restore $\Delta\Psi m$ during hypoxic stress (Fig. 4 E, F). In addition, we expressed a plasmid-based fluorescent protein kinase A (PKA) biosensor in H9c2 cells, and treated with misoprostol. The misoprostol time course shown in Figure 3G, demonstrates that PKA activation peaks 30-m following misoprostol treatment, and returns to control levels within 2-h, indicative of the type of rapid response driven by cell surface receptor activation. These results indicate that EP_4 receptor-dependent activation of PKA might be a mechanism by which misoprostol prevents mitochondrial permeability transition.

To investigate whether PKA can inhibit Bnip3 function by direct phosphorylation, we performed *in silico* analysis of the mouse Bnip3 amino acid sequence, which identified two conserved potential PKA phosphorylation motifs, the first at Ser-107 and the second at Thr-181. We engineered peptides spanning each of these regions and exposed them to in vitro kinase reaction with purified PKA. Following the kinase reaction, peptides were analyzed by mass spectrometry. For the peptides spanning Ser-107, no discernible phosphorylation ions were observed (Supp Fig. 4 A). However, for the peptides spanning Thr-181, a single ion monitoring (SIM) scan of the the control peptide displayed a predominant peak at m/z of 836.92 (z = 2+); however, following kinase reaction the peptide showed an increased m/z of 40, representing the addition of a phosphate to the peptide (Mass = 80.00 Da)(Figure 4H). We also evaluated if this peptide could phosphorylated at more then one residue, but we did not detect an increased m/z of 80 (ie. 160 Da)(Supp Fig. 4 B) Next, we analyzed the MS^2 spectra produced by collision-induced dissociation (CID) of the mass-shifted ion with m/z = 876.86 (z=2+). CID typically fragments phospho-peptides resulting in the neutral loss of H_3PO_4, and the generation of a product-ion with a mass less 98 Da (m/z = 49 for z=2+). CID of the phospho-peptide spanning Thr-181 yielded a product-ion with m/z = 827.92 (delta = 48.94), indicating phosphorylation (Figure 4I). Although these mass shifts are consistent with phosphorylation, they do not identify which of the serines or threonines are phosphorylated within the peptide. Thus, we subjected the triply charged phospho-peptide (m/z=585.27) spanning Thr-181 to electron transfer dissociation (ETD). This technique breaks peptide bonds, but retains side-chain phosphorylations to

determine specific phospho-residues. Using the MS^2 spectra produced by ETD, Mascot software definitively identified threonine-181 of Bnip3 as the phosphorylation residue (Fig. 4J).

To confirm that PKA phosphorylates Bnip3 in cells and *in vivo*, we used a custom phospho-specific antibody targeted to Thr-181. We co-expressed the catalytic subunit of PKA and Bnip3 in H9c2 cells and observed a marked increase in phosphorylation (p-Bnip3)(Fig. 4 K). We next exposed H9c2 cells to misoprostol overnight and observed an increase in endogenous p-Bnip3 at Thr-181. Finally, to determine if Bnip3 phosphorylation is regulated during hypoxia-induced cardiac pathologies, we performed western blots on cardiac extracts from neonatal mice exposed to hypoxia for 7 days, and observed a significant reduction of Bnip3 phosphorylation at Thr-181, suggesting an increase in Bnip3 activity in the hypoxic neonatal heart (Fig. 4 M, N). In addition, when the neonatal mice were exposed to both hypoxia and treated with misoprostol, Bnip3 phosphorylation was returned to control levels (Fig. 4 M, N). We further evaluated Bnip3 phosphorylation in adult rodent heart, and observed a significant decrease in Bnip3 phosphorylation in the viable border zone following 4-weeks of coronary ligation (C.L) in adult Sprague Dawley rats (Supplement 3 A-C). However, during the recovery phase (8 weeks post C.L.), where the heart is overcoming the initial insult, we observed a restoration in Bnip3 phosphorylation when compared to the sham control (Supplement 3 A-C). Taken together these results imply that Bnip3 phosphorylation at Thr-181 is a regulated event during hypoxic injury *in vivo*.

3.5. Misoprostol-induced cytoprotection is Thr-181 dependent.

To understand the cellular role of Bnip3 phosphorylation, we first engineered a peptide spanning Thr-181 and generated a Bnip3 expression plasmid containing neutral alanine mutations at Thr-181 (T181A). Using ion-trap mass spectroscopy combined with an *in vitro* kinase assay, we demonstrated that the Bnip3 mutant peptide can no longer be phosphorylated (Fig. 5 A), unlike its wild-type peptide shown previously (Fig. 4 H). To demonstrate specificity, we also engineered a peptide containing a neutral alanine at Thr-182, and observed near complete phosphorylation, similar to the wild-type peptide (Supp Fig. 4 C). We next employed gain-of-function transfection studies with the Bnip3-T181A construct in combination with mito-Emerald to visualize mitochondrial morphology. Similar to what was observed with the WT

Bnip3 construct, expression of the T181A mutant resulted in a robust shift in mitochondrial morphology towards a fragmented and punctate phenotype (Fig. 5 B, C). However, unlike WT Bnip3, the T181A mutant was not inhibited by misoprostol treatment, and the fragmented mitochondrial morphology was retained (Fig. 5 B, C). In addition, misoprostol was not able to overcome the significant reductions in ΔΨm that resulted from T181A expression in H9c2 cells (Fig. 5 D, E). To determine the specificity of Thr-181 as a down-stream target of misoprostol treatment, we reconstituted WT or T181A Bnip3 expression in Bnip3-null MEFs. We observed that both the WT and T181A constructs reduced mitochondrial membrane potential; however, misoprostol treatment restored ΔΨm to control in the WT Bnip3 transfected cells, but failed to significantly improve ΔΨm in the presence of T181A (Fig. 5 F, G).

When we investigated that underlying calcium phenomena, we observed that like WT, T181A expression shifted calcium away from the ER and into the mitochondria. However unlike WT, misoprostol was unable to prevent this calcium movement upstream of the ER in the presence of the T181A mutant (Fig. 5 H-K). Furthermore, using calcein-$CoCl_2$ and Live/Dead imaging, we observed that the T181A mutant was sufficient to drive mitochondrial permeability transition and cell death, which could not be prevented with misoprostol drug treatment (Fig. 5 L, M). These data demonstrate that phosphorylation of Bnip3 at threonine-181 is necessary for misoprostol to inhibit cellular Bnip3 function.

3.6. Misoprostol promotes survival by retaining phosphorylated Bnip3 in the cytosol.

To determine how phosphorylation at threonine-181 inhibits Bnip3 function, we differentially expressed mitochondrial matrix-targeted or ER-targeted green fluorescent plasmids in H9c2 cells, and performed immunofluorescence for Bnip3 following exposure to hypoxia and misoprostol. As shown in Figure 6 A, B and C, confocal microscopy revealed that at baseline there is very little interaction between the organelle-targeted fluorophores and Bnip3, however when H9c2 cells are exposed to hypoxia the colocalization coefficient is increased by more than 116.3% and 381.9% at the mitochondria and ER, respectively. Interestingly, we observed that this organellar localization was abrogated with the addition of misoprostol treatment (Fig. 6 A-C). Next, we determined the subcellular localization of phosphorylated Bnip3 through subcellular fractionation studies. We observed that Bnip3 is predominantly localized to the

mitochondria, and to a lesser extent at the ER, while phosphorylated Bnip3 is retained in the cytosol (Fig. 6 D), a location commonly associated with Bnip3 inactivativation (Azad *et al*, 2008).

In silico analysis of Bnip3 predicted that threonine-181 lies within a conserved interacting domain of the molecular chaperone family 14-3-3, which recognizes motifs commonly found within PKA and CaMKII phosphorylation sites. As certain 14-3-3 family members are known interactors with Bcl-2 proteins (Datta *et al*, 2000; Masters & Fu, 2001; Petosa *et al*, 1998; Tzivion & Avruch, 2002; Tan *et al*, 2000), we investigated the role of these molecular chaperones as a mechanism by which misoprostol inhibits Bnip3 function. Using hypoxia and misoprostol exposed PVNCs, we applied BvO2, a pan-14-3-3 inhibitor, and assessed mitochondrial membrane potential using TMRM. We observed that misoprostol's ability to to rescue of $\Delta\Psi m$ was prevented with 14-3-3 inhibition (Fig. 6 E). We observed similar results when we used calcein-$CoCl_2$ to visualize MPT, where misoprostol treatment prevented hypoxia-induced permeability transition, which was prevented with the addition of BvO2 (Fig. 6 F, G).

We were further interested in determining which 14-3-3 family member is involved in this mechanism. Based on previous data from our group, which demonstrated that 14-3-3β traffics phosphorylated Nix (Bnip3L) from the mitochondria and ER/SR in skeletal muscle cell lines, we began by investigating this 14-3-3 family member in the cardiomyocyte (da Silva Rosa *et al*, 2019). Using gain of function transfection studies where we expressed Bnip3 and 14-3-3β, alone and in combination, in H9c2 cells. TMRM staining revealed that like misoprostol, 14-3-3β was able to rescue Bnip3-induced mitochondrial depolarizations (Fig. 6 H, I). Similar experiments were conducted using 14-3-3ε, which was unable to restore mitochondrial membrane potential, demonstrating some degree of isoform specificity (Fig. 6 J). Next, we determined that 14-3-3β expression is sufficient to prevent the ER calcium depletion and mitochondrial calcium accumulation that is triggered by Bnip3 expression (Fig. 6 K-M). Using the calcein-$CoCl_2$ method, we also evaluated how these calcium events were affecting MPT. Similar to our previous results, Bnip3 significantly increases the number of H9c2 cells experiencing MPT in each field, reducing the number of cells with distinct mitochondrial puncta. However, consistent with the mitochondrial calcium

results, when we combined Bnip3 and 14-3-3β expression, MPT was prevented and cells returned to their normal punctate phenotype (Fig. 6 N, O).

Given this data indicating a potential functional interaction between 14-3-3β and Bnip3, we were next interested in determining if there was a physical interaction between the two proteins. In order to do this we co-expressed HA-14-3-3β and myc-Bnip3 in HCT-116 cells and performed a co-immunoprecitiatatiom with the HA antibody. Using this approach we observed a marked increase in detectable myc-Bnip3 when the two proteins were expressed together, indicative of a physical interaction between the two proteins (Fig. 6 P). Collectively, this data indicates that misoprostol promotes Bnip3 trafficking away from the mitochondria and ER through a mechanism involving 14-3-3 the molecular chaperones.

3.7 Bnip3 ablation prevents hypoxia-induced contractile dysfunction in vivo.

To determine if a direct link existed between hypoxia-induced alterations in contractile function and Bnip3 protein expression *in vivo*, we returned to our mouse model of neonatal hypoxia this time using previously characterized mice harboring a genetic deletion of Bnip3 (Diwan *et al*, 2007). Using this approach in combination with transthoracic echocardiography, we observed that hypoxia induces significant contractile dysfunction in wild-type PND10 animals, including reductions in ejection fraction (EF), and alterations in left ventricular filling between heart beats (E'/A') (Fig. 7 A-C). When we assessed Bnip3-null mice under that same conditions, there were no alterations in contractile function at baseline (normoxia) and the loss of Bnip3 conferred protection against hypoxia-induced derangements in contraction, preventing reductions in both EF and E'/A' (Fig. 7 A-C). These results phenocopy what we observed using misoprostol drug treatments during neonatal hypoxia, and indicates that the presence of functionally active Bnip3 is deleterious to contractile performance in the hypoxia-exposed neonatal heart.

4. Discussion:

Among the leading complications associated with preterm birth, systemic hypoxia affects an estimated 9 million infants a year and is a known driver of functional alterations in the developing heart. While until now the mechanisms have remained unclear, in this study we provide *in vivo, in vitro,* and

cell-based evidence, including data from human iPSC-derived cardiomyocytes, that hypoxia-induced mitochondrial dysfunction and bioenergetic collapse is a major driver of this neonatal cardiac dysfunction. Through several lines of investigation, including being the first study of its kind to assess the effect of Bnip3 genetic ablation in the neonatal heart, we established that this pathology is contingent on Bnip3 protein expression. We further demonstrate that Bnip3 underpins this pathology through driving mitochondrial calcium accumulation and oxidative-phosphorylation failure, ultimately resulting in ROS production, MPT and cell death. We also demonstrate that Bnip3 activity can be pharmacologically modulated through PGE1-induced activation of EP_4 receptors, resulting in PKA signalling, phosphorylation of Bnip3 at threonine-181, and prevention of hypoxia-induced mitochondrial dysfunction.

The results presented in this report serve to unify previous reports demonstrating the deleterious role of Bnip3 and its pro-death C-terminal transmembrane (TM) domain. Through detailed evaluations of the role of Bnip3 at ER/SR, we demonstrate changes in subcellular calcium localization. Previous data suggests that the TM domain of Bnip3 directly interacts with Bcl-2, which is traditionally associated with inhibiting the IP_3R, resulting in calcium release from the ER (Ray *et al*, 2000). This Bnip3-induced ER calcium is quickly buffered by the mitochondria through VDAC and MCU directly in the mitochondrial matrix (Rapizzi *et al*, 2002; Chaudhuri *et al*, 2013; Baughman *et al*, 2011). These previous studies further demonstrate that mitochondrial calcium drives a loss of membrane potential and respiration, ROS production, MPT and ultimately a caspase-independent necrosis (Ray *et al*, 2000; Vande Velde *et al*, 2000; Zhang *et al*, 2009). However, Bnip3 is known as a dual-regulator of cell death, where it also inserts through the outer mitochondrial membrane and uses its TM domain to interact with the dynamin related protein, OPA-1 (Landes *et al*, 2010; Chen *et al*, 2010; Pereira *et al*, 2017). While OPA-1 is traditionally associated with maintaining cristae structure, efficient organization of ETC complexes, and mitochondrial fusion, disruption and/or genetic deletion of OPA-1 results in ETC dysfunction, mitochondrial fragmentation and cell death (Frezza *et al*, 2006; Cogliati *et al*, 2013; Liu & Frazier, 2015). Additionally, work by Rikka *et al.* demonstrated that cardiomyocyte-specific overexpression of Bnip3 enhances

mitochondrial protease activity, resulting in the degradation of complex-1 (NADH ubiquinone oxidoreductase) and -4 (cytochrome c oxidase), suppressing respiratory activity, while enhancing mitochondrial fragmentation (Rikka et al, 2011). ETC dysfunction is further tied to the overproduction of mitochondrial reactive oxygen species, which propagates an influx of calcium into the matrix (Lopez-Fabuel *et al*, 2016; Koopman *et al*, 2007). Together these studies demonstrate that by altering mitochondrial function and calcium homeostasis in two very different ways, Bnip3 displays overlapping and redundant functions to depress energy production and promote necrotic cell death in the heart.

Consistent with these studies, we show that in the context of neonatal pathological hypoxia signaling, Bnip3 expression in the heart drives mitochondrial dysfunction and cell death. By directly measuring SR/ER calcium content this work advances our understanding of what Bnip3 is doing at the organellar level, and supports the notion that Bnip3 triggers ER calcium release that is buffered by the mitochondria. We further build on the findings of these past studies that link mitochondrial calcium accumulation with ROS production alongside the induction of MPT, bioenergetic collapse and necrosis both in cultured cardiomyocytes and *in vivo*. Importantly the work presented here also demonstrates that these pathways can be pharmacologically modulated through PGE1-induced EP4 activation, which work from us and others, has been shown to be cardioprotective (Field *et al*, 2018; Martens *et al*, 2020; Bryson *et al*, 2018). While a previous study has demonstrated that Bnip3 phosphorylation inhibits its interactions with OPA-1, we provide mechanistic evidence both *in vivo* and in cardiomyocytes that misoprostol activates the EP4 receptor and PKA, resulting in an inhibitory phosphorylation of Bnip3's TM domain at Thr-181. Furthermore, based on the known roles of the 14-3-3 family of molecular chaperones, we propose a mechanism by which 14-3-3β translocates Bnip3 to the cytosol, which likely prevents interactions with factors at ER and mitochondrial, including Bcl-2 and OPA-1, respectively (Datta *et al*, 2000; Masters & Fu, 2001; Petosa *et al*, 1998; Tzivion & Avruch, 2002; Tan *et al*, 2000).

Taken together the results presented in this study elevate the role of Bnip3 in the neonatal heart, and strongly implicate it as a critical regulator of mitochondrial calcium homeostasis that when upregulated by hypoxia in the neonatal heart drives calcium into the mitochondria and a necrotic

phenotype. Additionally, the data in this preclinical study builds on the accumulating evidence that misoprostol directly regulates Bnip3 activity, with potential meaningful implications for neonatal and adult hypoxia-induced cardiac pathologies, and stem cell-based cardiac therapies where promoting cardiomyocyte survival would be of benefit.

Author Contributions:

M.D.M. and J.W.G. conceptualized the study. M.D.M. and J.W.G. were responsible for writing the paper. M.D.M. designed and conducted most of the investigations and was responsible for data curation. M.D.M. was also responsible for formal analysis and data visualization. N.S. conducted both the Seahorse XF-24 investigation and cellular/cardiac ATP assays, including data curation and formal analysis. D.C. conducted the Bnip3 qRT-PCR investigations. B.X. conducted PND10 *in vivo* transthoracic echocardiography. C.R. and J.W.G designed and conducted ion-trap mass spec studies. J.M.K. and A.M. conducted isolated mitochondrial studies. I.M.D. and S.R. designed and conducted M.I. model. J.W.G., and A.R.W. were responsible for funding acquisition. All authors reviewed the results, edited, and approved the final version of the manuscript.

Disclosures and Conflicts:

None.

Acknowledgments:

This work was supported by the Natural Science and Engineering Research Council (NSERC) Canada, through Discovery Grants to J.W.G. and A.R.W.. This work is supported by Heart and Stroke Foundation of Canada (HSFC) Grants to J.W.G. and G.M.H. V.W.D and C.A.D. are supported by CIHR. G.M.H is a Canada Research Chair in Cardiolipin Metabolism. M.D.M. and N.S. are supported by studentships from the Children's Hospital Foundation of Manitoba and Research Manitoba, M.D.M. received support from the DEVOTION research cluster. A.S. is supported by grants from SSHRC New Frontiers in Research Fund, Research Manitoba, Children's Hospital Research Institute of Manitoba, and Children's Hospital Foundation. We thank Dr. 's Bill Diehl-Jones and Yan Hai for their support during the preliminary phase of this study. We also thank Farhana Begum from the Histomorphology and Ultrastructural Imaging Core

in the Department of Human Anatomy and Cell Science at the University of Manitoba for her technical expertise that made this work possible. This work was conducted at the Children's Hospital Research Institute of Manitoba.

References:

Armstrong K, Franklin O, Sweetman D & Molloy EJ (2012) Cardiovascular dysfunction in infants with neonatal encephalopathy. *Arch Dis Child* 97: 372–375

Azad MB, Chen Y, Henson ES, Cizeau J, McMillan-Ward E, Israels SJ & Gibson SB (2008) Hypoxia induces autophagic cell death in apoptosis-competent cells through a mechanism involving BNIP3. *Autophagy* 4: 195–204

Baines CP, Kaiser RA, Purcell NH, Blair NS, Osinska H, Hambleton MA, Brunskill EW, Sayen MR, Gottlieb RA, Dorn GW, *et al* (2005) Loss of cyclophilin D reveals a critical role for mitochondrial permeability transition in cell death. *Nature* 434: 658–662

Baughman JM, Perocchi F, Girgis HS, Plovanich M, Belcher-Timme CA, Sancak Y, Bao XR, Strittmatter L, Goldberger O, Bogorad RL, *et al* (2011) Integrative genomics identifies MCU as an essential component of the mitochondrial calcium uniporter. *Nature* 476: 341–345

Blencowe H, Cousens S, Oestergaard MZ, Chou D, Moller A-B, Narwal R, Adler A, Vera Garcia C, Rohde S, Say L, *et al* (2012) National, regional, and worldwide estimates of preterm birth rates in the year 2010 with time trends since 1990 for selected countries: a systematic analysis and implications. *The Lancet* 379: 2162–2172

Bryson TD, Gu X, Khalil RM, Khan S, Zhu L, Xu J, Peterson E, Yang X-P & Harding P (2018) Overexpression of prostaglandin E2 EP4 receptor improves cardiac function after myocardial infarction. *J Mol Cell Cardiol* 118: 1–12

Bryson TD, Pandrangi TS, Khan SZ, Xu J, Pavlov TS, Ortiz PA, Peterson EL & Harding P (2020) The Deleterious Role of the Prostaglandin E2 EP3 Receptor in Angiotensin II Hypertension. *Am J Physiol-Heart Circ Physiol*: ajpheart.00538.2019

Carmeliet P, Dor Y, Herbert J-M, Fukumura D, Brusselmans K, Dewerchin M, Neeman M, Bono F, Abramovitch R, Maxwell P, *et al* (1998) Role of HIF-1α in hypoxia-mediated apoptosis, cell proliferation and tumour angiogenesis. *Nature* 394: 485–490

Chaudhuri D, Sancak Y, Mootha VK & Clapham DE (2013) MCU encodes the pore conducting mitochondrial calcium currents. *eLife* 2

Chaudhuri RD, Banerjee D, Banik A & Sarkar S (2020) Severity and duration of hypoxic stress differentially regulates HIF-1α-mediated cardiomyocyte apoptotic signaling milieu during myocardial infarction. *Arch Biochem Biophys*: 108430

Chen Y, Lewis W, Diwan A, Cheng EH-Y, Matkovich SJ & Dorn GW (2010) Dual autonomous mitochondrial cell death pathways are activated by Nix/BNip3L and induce cardiomyopathy. *Proc Natl Acad Sci* 107: 9035–9042

Cogliati S, Frezza C, Soriano ME, Varanita T, Quintana-Cabrera R, Corrado M, Cipolat S, Costa V, Casarin A, Gomes LC, *et al* (2013) Mitochondrial Cristae Shape Determines Respiratory Chain Supercomplexes Assembly and Respiratory Efficiency. *Cell* 155: 160–171

Datta SR, Katsov a, Hu L, Petros a, Fesik SW, Yaffe MB & Greenberg ME (2000) 14-3-3 proteins and survival kinases cooperate to inactivate BAD by BH3 domain phosphorylation. *Mol Cell* 6: 41–51

Diehl-Jones W, Archibald A, Gordon JW, Mughal W, Hossain Z & Friel JK (2015) Human Milk Fortification Increases Bnip3 Expression Associated With Intestinal Cell Death In Vitro. *J Pediatr Gastroenterol Nutr* 61: 583–590

Ding Y, Li J, Enterina JR, Shen Y, Zhang I, Tewson PH, Mo GCH, Zhang J, Quinn AM, Hughes TE, *et al* (2015) Ratiometric biosensors based on dimerization-dependent fluorescent protein exchange. *Nat Methods* 12: 195–198

Diwan A, Krenz M, Syed FM, Wansapura J, Ren X, Koesters AG, Li H, Kirshenbaum LA, Hahn HS, Robbins J, *et al* (2007) Inhibition of ischemic cardiomyocyte apoptosis through targeted ablation of Bnip3 restrains postinfarction remodeling in mice. *J Clin Invest* 117: 2825–2833

Dixon IM, Lee SL & Dhalla NS (1990) Nitrendipine binding in congestive heart failure due to myocardial infarction. *Circ Res* 66: 782–788

Dolinsky VW, Morton JS, Oka T, Robillard-Frayne I, Bagdan M, Lopaschuk GD, Des Rosiers C, Walsh K, Davidge ST & Dyck JRB (2010) Calorie Restriction Prevents Hypertension and Cardiac Hypertrophy in the Spontaneously Hypertensive Rat. *Hypertension* 56: 412–421

Field JT, Martens MD, Mughal W, Hai Y, Chapman D, Hatch GM, Ivanco TL, Diehl-Jones W & Gordon JW (2018) Misoprostol regulates Bnip3 repression and alternative splicing to control cellular calcium homeostasis during hypoxic stress. *Cell Death Discov* 4: 98–98

Frezza C, Cipolat S, Martins de Brito O, Micaroni M, Beznoussenko GV, Rudka T, Bartoli D, Polishuck RS, Danial NN, De Strooper B, *et al* (2006) OPA1 Controls Apoptotic Cristae Remodeling Independently from Mitochondrial Fusion. *Cell* 126: 177–189

Galluzzi L, Vitale I, Aaronson SA, Abrams JM, Adam D, Agostinis P, Alnemri ES, Altucci L, Amelio I, Andrews DW, *et al* (2018) Molecular mechanisms of cell death: recommendations of the Nomenclature Committee on Cell Death 2018. *Cell Death Differ* 25: 486–541

Ghavami S, Cunnington RH, Gupta S, Yeganeh B, Filomeno KL, Freed DH, Chen S, Klonisch T, Halayko AJ, Ambrose E, *et al* (2015) Autophagy is a regulator of TGF-β1-induced fibrogenesis in primary human atrial myofibroblasts. *Cell Death Dis* 6: e1696

Giorgio V, von Stockum S, Antoniel M, Fabbro A, Fogolari F, Forte M, Glick GD, Petronilli V, Zoratti M, Szabo I, *et al* (2013) Dimers of mitochondrial ATP synthase form the permeability transition pore. *Proc Natl Acad Sci* 110: 5887–5892

Gordon JW, Shaw JA & Kirshenbaum LA (2011) Multiple facets of NF-kB in the heart: To be or not to NF-kB. *Circ Res* 108: 1122–1132

Greer SN, Metcalf JL, Wang Y & Ohh M (2012) The updated biology of hypoxia-inducible factor. *EMBO J* 31: 2448–2460

Gustafsson ÅB (2011) Bnip3 as a dual regulator of mitochondrial turnover and cell death in the myocardium. *Pediatr Cardiol* 32: 267–274

Hamacher-Brady A, Brady NR, Logue SE, Sayen MR, Jinno M, Kirshenbaum LA, Gottlieb RA & Gustafsson ÅB (2007) Response to myocardial ischemia/reperfusion injury involves Bnip3 and autophagy. *Cell Death Differ* 14: 146–157

Izzo V, Bravo-San Pedro JM, Sica V, Kroemer G & Galluzzi L (2016) Mitochondrial Permeability Transition: New Findings and Persisting Uncertainties. *Trends Cell Biol* 26: 655–667

Karch J, Bround MJ, Khalil H, Sargent MA, Latchman N, Terada N, Peixoto PM & Molkentin JD (2019) Inhibition of mitochondrial permeability transition by deletion of the ANT family and CypD. *Sci Adv* 5

Karch J, Kwong JQ, Burr AR, Sargent MA, Elrod JW, Peixoto PM, Martinez-Caballero S, Osinska H, Cheng EH-Y, Robbins J, *et al* (2013) Bax and Bak function as the outer membrane component of the mitochondrial permeability pore in regulating necrotic cell death in mice. *eLife* 2

Koopman WJH, Verkaart S, Visch HJ, van Emst-de Vries S, Nijtmans LGJ, Smeitink JAM & Willems PHGM (2007) Human NADH:ubiquinone oxidoreductase deficiency: radical changes in mitochondrial morphology? *Am J Physiol-Cell Physiol* 293: C22–C29

Kotera I, Iwasaki T, Imamura H, Noji H & Nagai T (2010) Reversible Dimerization of *Aequorea victoria* Fluorescent Proteins Increases the Dynamic Range of FRET-Based Indicators. *ACS Chem Biol* 5: 215–222

Kubasiak LA, Hernandez OM, Bishopric NH & Webster KA (2002) Hypoxia and acidosis activate cardiac myocyte death through the Bcl-2 family protein BNIP3. *Proc Natl Acad Sci* 99: 12825–12830

Kubli DA, Ycaza JE & Gustafsson ÅB (2007) Bnip3 mediates mitochondrial dysfunction and cell death through Bax and Bak. *Biochem J* 405: 407–415

Kwong JQ, Davis J, Baines CP, Sargent MA, Karch J, Wang X, Huang T & Molkentin JD (2014) Genetic deletion of the mitochondrial phosphate carrier desensitizes the mitochondrial permeability transition pore and causes cardiomyopathy. *Cell Death Differ* 21: 1209–1217

Landes T, Emorine LJ, Courilleau D, Rojo M, Belenguer P & Arnauné-Pelloquin L (2010) The BH3-only Bnip3 binds to the dynamin Opa1 to promote mitochondrial fragmentation and apoptosis by distinct mechanisms. *EMBO Rep* 11: 459–465

Liu KE & Frazier WA (2015) Phosphorylation of the BNIP3 C-terminus inhibits mitochondrial damage and cell death without blocking autophagy. *PLoS ONE* 10: 1–28

Liu L, Oza S, Hogan D, Chu Y, Perin J, Zhu J, Lawn JE, Cousens S, Mathers C & Black RE (2016) Global, regional, and national causes of under-5 mortality in 2000–15: an updated systematic analysis with implications for the Sustainable Development Goals. *The Lancet* 388: 3027–3035

Lopez-Fabuel I, Le Douce J, Logan A, James AM, Bonvento G, Murphy MP, Almeida A & Bolaños JP (2016) Complex I assembly into supercomplexes determines differential mitochondrial ROS production in neurons and astrocytes. *Proc Natl Acad Sci* 113: 13063–13068

Luu TM, Katz SL, Leeson P, Thebaud B & Nuyt A-M (2015) Preterm birth: risk factor for early-onset chronic diseases. *Can Med Assoc J*: 1–5

Martens MD, Field JT, Seshadri N, Day C, Chapman D, Keijzer R, Doucette CA, Hatch GM, West AR, Ivanco TL, *et al* (2020) Misoprostol attenuates neonatal cardiomyocyte proliferation through Bnip3, perinuclear calcium signaling, and inhibition of glycolysis. *J Mol Cell Cardiol* 146: 19–31

Masters SC & Fu H (2001) 14-3-3 Proteins Mediate an Essential Anti-apoptotic Signal. *J Biol Chem* 276: 45193–45200

Moghadam AR, da Silva Rosa SC, Samiei E, Alizadeh J, Field J, Kawalec P, Thliveris J, Akbari M, Ghavami S & Gordon JW (2018) Autophagy modulates temozolomide-induced cell death in alveolar Rhabdomyosarcoma cells. *Cell Death Discov* 4: 52

Mughal W, Martens M, Field J, Chapman D, Huang J, Rattan S, Hai Y, Cheung KG, Kereliuk S, West AR, *et al* (2018) Myocardin regulates mitochondrial calcium homeostasis and prevents permeability transition. *Cell Death Differ* 25: 1732–1748

Mughal W, Nguyen L, Pustylnik S, da Silva Rosa SC, Piotrowski S, Chapman D, Du M, Alli NS, Grigull J, Halayko AJ, *et al* (2015) A conserved MADS-box phosphorylation motif regulates differentiation and mitochondrial function in skeletal, cardiac, and smooth muscle cells. *Cell Death Dis* 6: e1944–e1944

Nakagawa T, Shimizu S, Watanabe T, Yamaguchi O, Otsu K, Yamagata H, Inohara H, Kubo T & Tsujimoto Y (2005) Cyclophilin D-dependent mitochondrial permeability transition regulates some necrotic but not apoptotic cell death. *Nature* 434: 652–658

Pereira RO, Tadinada SM, Zasadny FM, Oliveira KJ, Pires KMP, Olvera A, Jeffers J, Souvenir R, Mcglauflin R, Seei A, *et al* (2017) OPA1 deficiency promotes secretion of FGF21 from muscle that prevents obesity and insulin resistance. *EMBO J* 36: 2126–2145

Petosa C, Masters SC, Bankston LA, Pohl J, Wang B, Fu H & Liddington RC (1998) 14-3-3z Binds a Phosphorylated Raf Peptide and an Unphosphorylated Peptide Via Its Conserved Amphiphatic Groove. *J Biol Chem* 273: 16305–16310

Planchon TA, Gao L, Milkie DE, Davidson MW, Galbraith JA, Galbraith CG & Betzig E (2011) Rapid three-dimensional isotropic imaging of living cells using Bessel beam plane illumination. *Nat Methods* 8: 417–423

Rapizzi E, Pinton P, Szabadkai G, Wieckowski MR, Vandecasteele G, Baird G, Tuft RA, Fogarty KE & Rizzuto R (2002) Recombinant expression of the voltage-dependent anion channel enhances the transfer of Ca2+ microdomains to mitochondria. *J Cell Biol* 159: 613–624

Ray R, Chen G, Vande Velde C, Cizeau J, Park JH, Reed JC, Gietz RD & Greenberg AH (2000) BNIP3 Heterodimerizes with Bcl-2/Bcl-XL and Induces Cell Death Independent of a Bcl-2 Homology 3 (BH3) Domain at Both Mitochondrial and Nonmitochondrial Sites. *J Biol Chem* 275: 1439–1448

Regula KM, Ens K & Kirshenbaum LA (2002) Inducible expression of BNIP3 provokes mitochondrial defects and hypoxia-mediated cell death of ventricular myocytes. *Circ Res* 91: 226–231

Rikka S, Quinsay MN, Thomas RL, Kubli DA, Zhang X, Murphy AN & Gustafsson ÅB (2011) Bnip3 impairs mitochondrial bioenergetics and stimulates mitochondrial turnover. *Cell Death Differ* 18: 721–731

Seshadri N, Jonasson ME, Hunt KL, Xiang B, Cooper S, Wheeler MB, Dolinsky VW & Doucette CA (2017) Uncoupling protein 2 regulates daily rhythms of insulin secretion capacity in MIN6 cells and isolated islets from male mice. *Mol Metab* 6: 760–769

Shastri AT, Samarasekara S, Muniraman H & Clarke P (2012) Cardiac troponin i concentrations in neonates with hypoxic-ischaemic encephalopathy. *Acta Paediatr Int J Paediatr* 101: 26–29

da Silva Rosa SC, Martens MD, Field JT, Nguyen L, Kereliuk SM, Hai Y, Chapman D, Diehl-Jones W, Aliani M, West AR, *et al* (2019) Nix induced mitochondrial fission, mitophagy, and myocyte insulin resistance are abrogated by PKA phosphorylation Cell Biology

Tan Y, Demeter MR, Ruan H & Comb MJ (2000) BAD Ser-155 phosphorylation regulates BAD/Bcl-XL interaction and cell survival. *J Biol Chem* 275: 25865–25869

Tzivion G & Avruch J (2002) 14-3-3 Proteins: Active Cofactors in Cellular Regulation by Serine/Threonine Phosphorylation. *J Biol Chem* 277: 3061–3064

Vande Velde C, Cizeau J, Dubik D, Alimonti J, Brown T, Israels S, Hakem R & Greenberg AH (2000) BNIP3 and genetic control of necrosis-like cell death through the mitochondrial permeability transition pore. *Mol Cell Biol* 20: 5454–68

Vannucci SJ (2004) Hypoxia-ischemia in the immature brain. *J Exp Biol* 207: 3149–3154

Whelan RS, Kaplinskiy V & Kitsis RN (2010) Cell Death in the Pathogenesis of Heart Disease: Mechanisms and Significance. *Annu Rev Physiol* 72: 19–44

Wu J, Liu L, Matsuda T, Zhao Y, Rebane A, Drobizhev M, Chang YF, Araki S, Arai Y, March K, *et al* (2013) Improved orange and red Ca2+ indicators and photophysical considerations for optogenetic applications. *ACS Chem Neurosci* 4: 963–972

Zhang L, Li L, Liu H, Borowitz JL & Isom GE (2009) BNIP3 mediates cell death by different pathways following localization to endoplasmic reticulum and mitochondrion. *FASEB J* 23: 3405–3414

Figure Legends:

Figure 1. Misoprostol prevents hypoxia-induced contractile and mitochondrial dysfunction in vivo. **(A)** Fractional shortening, **(B)** Ejection fraction and **(C)** E'/A' ratio for 4-6 post-natal day (PND10) mice exposed to hypoxia (10% O_2) ± 10 µg/kg misoprostol daily from PND3-10 per group as determined by transthoracic echocardiography. **(D)** PCR-based array performed on RNA isolated from PND10 mouse ventricles (n=3 animals per group) treated as in (A), where green indicates a downregulation of expression (<1), and red indicates an upregulation of expression (>1), relative to the the normoxic control (1). **(E)** Relative Bnip3 gene expression from the PND10 mouse ventricles of animals (n=5-6 animals per group) treated as in (A). **(F)** Measurement of ATP content in PND10 mouse ventricles (n=6-8 animals per condition) treated as in (A). **(G)** Measurement of cardiac lactate content in the PND10 mouse ventricle (n=6-8 animals per condition) treated as in (A). **(H)** PND10 hearts treated as in (A) and imaged via transmission electron microscopy. Images showing mitochondrial morphology. All data are represented as

mean ± S.E.M. *P<0.05 compared with control, while **P<0.05 compared with hypoxia treatment, determined by 1-way ANOVA or 2-way ANOVA where appropriate.

Figure 2. Misoprostol prevents hypoxia-induced mitochondrial dysfunction *in vitro*. (A) Primary ventricular neonatal cardiomyocytes (PVNCs) treated with 10 μM misoprostol (Miso) ± 1% O_2 (HPX) for 24 hours. MitoView Green was included in all conditions to show mitochondrial morphology. Cells were stained with hoechst (blue) and imaged by standard fluorescence microscopy. **(B)** Quantification of cells in (A), where the number of cells with elongated and fragmented mitochondria are expressed as a percentage of all transfected cells in 30 random fields, across 3 independent experiments. **(C)** Quantification of PVNC's treated as in (A). Cells were stained with TMRM (red) and hoechst (blue) and imaged by standard fluorescence microscopy. Red fluorescent signal was normalized to cell area and quantified in 30 random fields, across 3 independent experiments. **(D)** Human induced pluripotent stem cell-derived cardiomyocytes (H-IPSC-CMs) treated as in (A). Cells were stained with TMRM (red) and hoechst (blue) and imaged by standard fluorescence microscopy. **(E)** Quantification of cells in (D), as in (C). **(F)** PVNC's treated as in (A). Cells were stained with MitoSOX (Red) and hoechst (blue) and imaged by standard fluorescence microscopy. **(G)** Quantification of cells in (F), as in (C). **(H)** Quantification of PVNC's treated as in (A). Cells were stained with dihyrorhod-2AM (Red) and hoechst (blue) and imaged by standard fluorescence microscopy and quantified as in (C). **(I)** H-IPSC-CMs treated as in (A). Cells were stained with dihyrorhod-2AM (Red) and hoechst (blue) and imaged by standard fluorescence microscopy. **(J)** Quantification of cells in (I), as in (C). **(K)** Quantification of PVNC's treated as in (A). Cells were stained with hoechst (blue) and calcein-AM quenched by cobalt chloride ($CoCl_2$, 5 μM) to assess permeability transition, where green fluorescent signal was normalized to cell area and quantified in 30 random fields, across 3 independent experiments. **(L)** Calculated oxygen consumption rates (OCR) determined by Seahorse Xf-24 analysis to evaluate mitochondrial function. **(M)** Quantification of PVNC's treated as in (A). Live cells were stained with calcein-AM (green), and necrotic cells were stained with ethidium homodimer-1 (red). Percent (%) dead was calculated across 30 random fields, across 3 independent experiments. **(N)** PVNC's treated as in (A). Cells were fixed, stained with hoechst (blue), and immunofluorescence was performed using a HMGB1

primary antibody (green). Cells were then imaged by standard fluorescence microscopy. **(O)** Quantification of cells in (N), as in (K). **(P)** Immunoblot of concentrated filtered media from PVNC's treated as in (A), and probed as indicated. All data are represented as mean ± S.E.M. **P*<0.05 compared with control, while ***P*<0.05 compared with hypoxia treatment, determined by 1-way ANOVA or 2-way ANOVA where appropriate.

Figure 3. Misoprostol prevents Bnip3-induced mitochondrial dysfunction and cell death. (A) PVNC's treated with 10 μM misoprostol (Miso) ± 1% O_2 (HPX) for 24 hours. Cells were fixed, stained with hoechst (blue), and immunofluorescence was performed using a Bnip3 primary antibody (green). Cells were then imaged by standard fluorescence microscopy. **(B)** Quantification of cells in (A), where green fluorescent signal was normalized to cell area and quantified in 30 random fields, across 3 independent experiments. **(C)** Immunoblot for Bnip3 in protein extracts from WT and Bnip3$^{-/-}$ MEFs treated as in (A). **(D)** Quantification of WT and Bnip3$^{-/-}$ mouse embryonic fibroblasts (MEFs) treated as in (A). Cells were stained with TMRM (red) and hoechst (blue) and imaged by standard fluorescence microscopy. Red fluorescent signal was normalized to cell area and quantified in 15 random fields, across 3 independent experiments. **(E)** WT and Bnip3$^{-/-}$ MEFs treated as in (A). Cells were stained with hoechst (blue) and dihydrorhod-2AM to stain mitochondrial calcium. **(F)** Quantification of (E) as in (D) in 15 random fields, across 3 independent experiments. **(G)** Quantification of WT and Bnip3$^{-/-}$ MEFs treated as in (A). Cells were stained with hoechst (blue) and calcein-AM quenched by cobalt chloride ($CoCl_2$, 5 μM) to assess permeability transition. Green fluorescent signal was normalized to cell area and quantified in 15 random fields, across 3 independent experiments. **(H)** H9c2 cells transfected with pcDNA3 (control) or Myc-Bnip3 and treated with 10 μM misoprostol (Miso) or PBS control for 16 hours. Mito-Emerald (green) was included in all conditions to show transfected cells and mitochondrial morphology. Cells were stained with hoechst (blue) and imaged by standard fluorescence microscopy. **(I)** Quantification of cells in (H), where the number of cells with elongated and fragmented mitochondria are expressed as a percentage of all transfected cells in 30 random fields, across 3 independent experiments. **(J)** H9c2 cells treated as in (H). CMV-GFP (outline) was included in all conditions to indicate transfected cells Cells were stained and imaged as in (D). **(K)** Quantification of

cells in (J) as in (D). **(L)** H9c2 cells treated as in (H). ER-LAR-GECO (red) was included in all conditions to indicate ER calcium content. Cells were stained and imaged as in (H). **(M)** Quantification of cells in (L) as in (D) in 30 random fields, across 3 independent experiments. **(N)** H9c2 cells treated as in (H). Mito-CAR-GECO (red) was included in all conditions to indicate mitochondrial calcium content. Cells were stained and imaged as in (D). **(O)** Quantification of cells in (N) as in (D) in 30 random fields, across 3 independent experiments. **(P)** Quantification of H9c2 cells treated as in (H) and CMV-ds.RED was included in all conditions to indicate transfected cells. Cells were stained, imaged and quantified as in (G) across 30 random fields, across 3 independent experiments. **(Q)** Quantification of H9c2's treated as in (H). ATeam was used to indicate cytosolic ATP content. Cells were imaged by FRET-based microscopy. FRET-YFP (ATP) signal was divided by the YFP (unbound biosensor) signal in 15 random fields across 3 independent experiments. **(R)** Quantification of H9c2 cells treated as in (H). Live cells were stained with calcein-AM (green), and necrotic cells were stained with ethidium homodimer-1 (red) and are expressed as percent (%) dead in 30 random fields, across 3 independent experiments. All data are represented as mean ± S.E.M. $*P<0.05$ compared with control, while $**P<0.05$ compared with hypoxia treatment, determined by 1-way ANOVA or 2-way ANOVA where appropriate.

Figure 4. Misoprostol modulates a novel PKA phosphorylation site on Bnip3 at Thr-181. (A) Mitochondrial calcium retention capacity (CRC) in isolated mitochondria exposed to 10 μM misoprostol (Miso) or PBS control. **(B)** Mitochondrial swelling assay in isolated mitochondria treated as in (A). **(C)** H9c2 cells exposed to 1% O_2 (HPX) or 21% O_2 (control) and treated with 10 μM misoprostol (Miso) or PBS control for 24 hours. 10 μM L161,982 was also included in half of the conditions. Cells were stained with TMRM (red) and hoechst (blue) and imaged by standard fluorescence microscopy. **(D)** Quantification of cells in (C), where red fluorescent signal was normalized to cell area and quantified in 30 random fields, across 3 independent experiments. **(E)** H9c2 cells treated, stained and imaged as in (C). 1 μM L798106 was also included in half of the conditions. **(F)** Quantification of cells in (E), as in (D). **(G)** Quantification of H9c2 cells transfected with pPHT-PKA and treated with 10 μM misoprostol for 0.5-h, 1-h, 2-h and 4-h. Cells were imaged by standard fluorescence microscopy and the ratio of green (active) to red (inactive)

fluorescent signal was measured, normalized to cell area, and quantified in 10 random fields. **(H)** SIM scan of the wild-type peptide spanning the PKA site of Bnip3. The unphosphorylated peptide has a 837 m/z (z=2+) (Left), putative phosphorylation showing an increased m/z of 20 that corresponds to PO3 (M = 80.00 Da) (Right). **(I)** MS^2 spectra following collision induced dissociation (CID) of the mass shifted ion from (h) yielding a product-ion consistent with a neutral loss of phosphate. **(J)** MS^2 spectra following electron transfer dissociation (ETD) of a triply charged mass-shifted ion following kinase reaction (not shown). Analysis of this fragmentation spectra confirmed that threonine-181 is the preferred phosphorylation residue. **(K)** Immunoblot of H9c2 cells transfected with Myc-Bnip3 and/or PKA for 16 hours. **(L)** Immunoblot for phospho-Bnip3(T181) in protein extracts from H9c2 cells treated with 10 μM misoprostol (Miso) or PBS control for 16 hours. **(M)** Representative immunoblot of heart protein extracts from post-natal day (PND10) mice exposed to hypoxia (10% O_2) ± 10 μg/kg misoprostol from PND3-10. Extracts were immunoblotted as indicated. **(N)** Phospho-Bnip3 densitometry for extracts in (M), representing an n of 3 male PND10 mouse hearts. All data are represented as mean ± S.E.M. **P*<0.05 compared with control, while ***P*<0.05 compared with hypoxia treatment, determined by 1-way ANOVA or 2-way ANOVA where appropriate.

Figure 5. Misoprostol-induced cardioprotection is Thr-181 dependent. (A) SIM scan of a mutated peptide where the PKA site at Threonine-181 is replaced with Alanine (left). On the right, phosphorylation of this mutate peptide is negligible at the predicted m/z that corresponds to the addition of a PO_3 (M = 80.00 Da). **(B)** H9c2 cells transfected with pcDNA3 (control) or Myc-T181A and treated with 10 μM misoprostol (Miso) or PBS control for 16 hours. Mito-Emerald (green) was included in all conditions to show transfected cells and mitochondrial morphology. Cells were stained with hoechst (blue) and imaged by standard fluorescence microscopy. **(C)** Quantification of cells in (B), where the number of cells with elongated and fragmented mitochondria are expressed as a percentage of all transfected cells in 30 random fields, across 3 independent experiments. **(D)** H9c2 cells treated as in (B). CMV-GFP (outline) was included in all conditions to indicate transfected cells Cells were stained with TMRM (red) and hoechst (blue) and imaged by standard fluorescence microscopy. **(E)** Quantification of cells in (D), where red fluorescent

signal was normalized to cell area and quantified in 30 random fields, across 3 independent experiments. **(F)** Bnip3$^{-/-}$ mouse embryonic fibroblasts (MEFs) treated as in (B) where either Myc-Bnips(WT) or Myc-Bnip3(T181A) was transfected in. Cells were stained with TMRM (red) and hoechst (blue) and imaged by standard fluorescence microscopy. **(G)** Quantification of cells in (F), where red fluorescent signal was normalized to cell area and quantified in 15 random fields, across 3 independent experiments. **(H)** H9c2 cells treated as in (B). ER-LAR-GECO (red) was included in all conditions to indicate ER calcium content. Cells were stained with hoechst (blue) and imaged by standard fluorescence microscopy. **(I)** Quantification of cells in (H) as in (E) in 30 random fields, across 3 independent experiments. **(J)** H9c2 cells treated as in (B). Mito-CAR-GECO (red) was included in all conditions to indicate mitochondrial calcium content. Cells were stained with hoechst (blue) and imaged by standard fluorescence microscopy. **(K)** Quantification of cells in (J) as in (E) in 30 random fields, across 3 independent experiments. **(L)** Quantification of H9c2 cells treated as in (B) and CMV-ds.RED was included in all conditions to indicate transfected cells. Cells were stained with hoechst (blue) and calcein-AM quenched by cobalt chloride ($CoCl_2$, 5 μM) to assess permeability transition. Quantification was done by calculating the percentage of cells with mitochondrial puncta in 30 random fields, across 3 independent experiments. **(M)** Quantification of H9c2 cells treated as in (B). Live cells were stained with calcein-AM (green), and necrotic cells were stained with ethidium homodimer-1 (red) and are expressed as percent (%) dead in 30 random fields, across 3 independent experiments. All data are represented as mean ± S.E.M. *P<0.05 compared with control, while **P<0.05 compared with hypoxia treatment, determined by 1-way ANOVA or 2-way ANOVA where appropriate.

Figure 6. Misoprostol promotes survival by retaining phosphorylated Bnip3 in the cytosol with 14-3-3β. (A) H9c2 cells treated with 10 μM misoprostol (Miso) ± 1% O_2 (HPX) for 24 hours. Myc-Bnip3 and Mito-Emerald (green) were included in each condition to visualize localization. Cells were fixed, stained with hoechst (blue), and immunofluorescence was performed using a Myc-tag primary antibody (Red). Cells were then imaged by standard confocal microscopy. **(B)** Quantification of cells in (A), where colocalization coefficient was calculated for 30 cells per condition across 10 random fields. **(C)** Quantification of H9c2 cells treated as in (A). ER-Emerald (green) was transfected in all conditions. Cells

were fixed, stained with hoechst (blue), and immunofluorescence was performed using a Myc-tag primary antibody (Red). Cells were then imaged by standard confocal microscopy. Colocalization coefficient was calculated for 30 cells per condition across 10 random fields. **(D)** Fractionation of control treated H9c2. Protein extracts were fractionated and immunoblotted, as indicated. **(E)** Quantification of primary ventricular neonatal cardiomyocytes (PVNCs) treated with 10 μM misoprostol (Miso) ± 1% O_2 (HPX) for 24 hours. 5 μM BvO2 was included in half of the conditions to inhibit 14-3-3 protein activity. Cells were stained with TMRM (red) and hoechst (blue) and imaged by standard fluorescence microscopy. Red fluorescent signal was normalized to cell area and quantified in 20 random fields, across 2 independent experiments. **(F)** PVNC's treated as in (E). Cells were stained with hoechst (blue) and calcein-AM quenched by cobalt chloride ($CoCl_2$, 5 μM) to assess permeability transition, and imaged by standard fluorescence microscopy. **(G)** Quantification of cells in (F), where the percentage of cells with mitochondrial puncta was calculated in 20 random fields, across 2 independent experiments. **(H)** H9c2 cells transfected with pcDNA3 (control) or Myc-Bnip3 with and without HA-14-3-3β. CMV-GFP (outline) was included in all conditions to indicate transfected cells Cells were stained with TMRM (red) and hoechst (blue) and imaged by standard fluorescence microscopy. **(I)** Quantification of cells in (H), where red fluorescent signal was normalized to cell area and quantified in 30 random fields, across 3 independent experiments. **(J)** Quanficatification of H9c2s treated as in (G), with and without 14-3-3ε. Cells were stained and imaged as in (H), and quantified as an (I) across 30 random fields, in 3 independent experiments. **(K)** H9c2's treated as in (H). ER-LAR-GECO (red) was included in all conditions to indicate ER calcium content. Cells were stained and imaged as in (H). **(L)** Quantification of cells in (K) as in (I) in 30 random fields, across 3 independent experiments. **(M)** H9c2's treated as in (H). Mito-CAR-GECO (red) was included in all conditions to indicate mitochondrial calcium content. Quantification performed as in (I) in 30 random fields, across 3 independent experiments. **(N)** H9c2's treated as in (H), and CMV-ds.RED was included in all conditions to indicate transfected cells. Cells were stained with hoechst (blue) and calcein-AM quenched by cobalt chloride ($CoCl_2$, 5 μM) to assess permeability transition. **(O)** Quantification of cells in (N), where the percentage of cells with mitochondrial puncta was calculated in 30 random fields,

across 3 independent experiments. **(P)** Co-immunoprecipitation of HCT-116 cells expressing HA-14-3-3 and Myc-Bnip3. Proteins were pulled down with Myc and probed for HA-tag. Immunoblot was probed as indicated. All data are represented as mean ± S.E.M. **P*<0.05 compared with control, while ***P*<0.05 compared with hypoxia treatment, determined by 1-way ANOVA or 2-way ANOVA where appropriate.

Figure 7. Bnip3 ablation prevents hypoxia-induced contractile dysfunction in vivo. (A) Post-natal day 2 (PND2) Bnip3-WT and Bnip3-null mice are exposed to hypoxia (10% O_2) from PND3-10, hearts were imaged and collected on PND10. **(B)** Ejection fraction and **(C)** E'/A' ratio for PND10 animals treated as in (A), in 3-5 mice per group, as determined by transthoracic echocardiography. All data are represented as mean ± S.E.M. **P*<0.05 compared with WT control, while ***P*<0.05 compared with WT hypoxia treatment, determined by 1-way ANOVA.